# Molecules versus Nanoparticles: Identifying a Reactive Molecular Intermediate in the Synthesis of Ternary Coinage Metal Chalcogenides

Sweta Gahlot, Erwann Jeanneau, Deobrat Singh, Pritam Kumar Panda, Yogendra Kumar Mishra, Rajeev Ahuja, Gilles Ledoux, Shashank Mishra

# Molecules Vs nanoparticles: Identifying a reactive molecular intermediate in the synthesis of ternary coinage metal chalcogenides

***Sweta Gahlot,[†] Erwann Jeanneau,[‡] Deobrat Singh,[♯] Pritam Kumar Panda,[♯] Yogendra Kumar Mishra,[§] Rajeev Ahuja,[♯] Gilles Ledoux,[‖] Shashank Mishra*[†]***

[†] Univ Lyon, Université Claude Bernard Lyon 1, CNRS, UMR 5256, Institut de Recherches sur la Catalyse et l'Environnement de Lyon (IRCELYON), 2 avenue Albert Einstein, 69626 Villeurbanne, France.

[‡] Univ Lyon, Université Claude Bernard Lyon 1, Centre de Diffractométrie Henri Longchambon, 5 rue de La Doua, 69100 Villeurbanne, France.

[♯] Condensed Matter Theory Group, Department of Physics and Astronomy, Uppsala University, Box 516, 75120 Uppsala, Sweden.

[§] Mads Clausen Institute, NanoSYD, University of Southern Denmark, Alsion 2, Denmark.

[‖] Univ Lyon, Université Claude Bernard Lyon 1, CNRS, Institut Lumière Matière (ILM), 69626 Villeurbanne, France.

ABSTRACT: Identification of reactive intermediates during molecule-to-nanoparticles transformation has a great significance in comprehending the mechanism of nanoparticles formation and, therefore, optimizing the synthetic conditions and properties of the formed products. We report here room temperature synthesis of AgCuSe nanoparticles from the reaction of ditertiarybutyl selenide with trifluoroacetates (TFA) of silver(I) and copper(II). The isolation and characterization of a molecular species during the course of this reaction, $[Ag_2Cu(TFA)_4(^tBu_2Se)_4]$ (**1**), which shows an extraordinary reactivity and interesting thermochromic behavior (blue at 0 °C and green at RT), confirmed that ternary metal selenide NPs are formed *via* this intermediate species. Similar reactions with related dialkyl chalcogenide $R_2E$ resulted in the isolation of molecular species of similar composition $[Ag_2Cu(TFA)_4(R_2E)_4]$ [R = $^t$Bu, E = S (**2**); R = Me, E = Se (**3**); R = Me, E = S (**4**)] which are stable at RT but can be converted to ternary metal chalcogenides at elevated temperature. DFT calculations confirm the kinetic instability of **1** and throw light on its thermochromic properties.

## Introduction

The coinage metal chalcogenide nanomaterials are currently under intense investigations for their various physical properties (low band gaps of 0.15-2.0 eV, low toxicity as compared to Pb- and Cd-containing chalcogenides, high absorption coefficients, NIR emission, etc.) and widespread applications (thermoelectrics, photovoltaic solar cells, photocatalysis, memory devices, nonlinear optics, energy storage, etc.).[1,2] In particular, the ternary silver copper chalcogenides, which have structures that favor high mobility of the ions, are fast emerging as interesting materials for the applications in thermoelectricity, photocatalysis and electrochemical devices (batteries, fuel cells, gas sensors, etc.).[3-6] Among these, AgCuSe exists in two phases: a

room-temperature β-AgCuSe phase having an orthorhombic structure and a high-temperature α-AgCuSe phase with a cubic structure.[3,4] The structure of β-phase consists of alternating layers of Ag and CuSe, whereas the high temperature α-phase is composed of $Ag^+$ and $Cu^+$ cations randomly distributed at tetrahedral sites of the face centered cubic (fcc) unit cell of Se atoms. The room-temperature structure of $Ag_3CuS_2$ is similar to that of $Ag_2S$ and contains silver ions in two different environment, i.e. octahedral and highly distorted tetrahedral. The copper atoms are linearly coordinated by two sulfur atoms and bridge the channels.[7] Although the nanometric forms of ternary metal chalcogenides have previously been synthesized by direct reaction of copper and silver salts with elemental selenium in the presence of $NaBH_4$,[4] transforming $Ag_2Se$ or $Cu_{2-x}Se$ NPs into ternary selenides under suitable conditions,[5,8] or thermolysis of suitable metal precursors at high temperature,[9,10] the difficulty in controlling the stoichiometry of the constituent elements often hinders the reproducibility in their synthesis .

Recently, dialkyl dichalcogenides ($R_2E_2$, where R = alkyl or aryl, E = S, Se, or Te) have been used as low temperature chalcogen sources for the solution-phase synthesis of metal chalcogenide nanocrystals.[11,12] These dialkyl dichalcogenides $R_2E_2$ not only possess relatively weak E−E bonds that can be readily cleaved under mild thermolytic or photolytic conditions but also their reactivity can be altered by varying organic substituents R on them. The above synthesis under mild conditions have enabled the isolation of metastable nanocrystalline phases with unusual composition and morphology. It has been reported that neat dialkyl diselenides could be thermally or photolytically decomposed to give elemental selenium, dialkylselenide ($R_2Se$), and/or organic byproducts *via* radical scission of the Se−Se and Se−R bonds.[13-15] These observations indicate that the dialkylselenide $R_2Se$ can be an interesting alternative selenium source for the synthesis of metal selenide nanocrystals under milder conditions because, in

addition to all the advantages that $R_2E_2$ possess (such as solubility, commercial availability, property optimization by varying the R, etc.), the dialkyl selenide $R_2Se$ has additional advantage that it bypasses the cleavage step of E-E in $R_2E_2$.

Solution routes to metal chalcogenide nanocrystals are vastly appealing not only because they are less energy intensive than vacuum techniques, and have the potential for scalability, but also due to the fact that one can exploit the advantage of dialkyl selenides as low temperature chalcogen sources in the solution phase, and therefore, may synthesize interesting metastable phases of metal chalcogenides.[11,12] Indeed, the silylated chalcogenoethers $(Me_3Si)_2E$ (E = S, Se, Te) have been used in the solution phase synthesis of metal chalcogenide nanomaterials,[16] although utilization of relatively less reactive non-silylated dialkyl chalcogenoethers $R_2E$ has been restricted to the elaboration of thin films in Chemical Vapor Deposition (CVD) technique that requires high temperature.[17-22] The use of non-silylated $R_2E$ ligands, which have high coordinating ability as compared to $R_2E_2$,[23-26] may potentially lead to isolation of intermediate molecular species which could throw light on the possible mechanism of molecule-to-nanoparticle transformation.[27,28] Starting with a well-defined precursors may also overcome the problem of controlling the stoichiometry of the constituent elements, which often hinders the reproducibility in the synthesis of ternary metal chalcogenides. In this work, we sought to explore divergent reactivity of $R_2E$ (E = Se, S: R = Me, $^t$Bu) with $Cu(TFA)_2$ and Ag(TFA) as a means to establish a well-defined chemical route for the mild synthesis of the ternary copper silver chalcogenide nanoparticles by attempting to isolate and characterize molecular intermediates on the way to materials in the solution phase.

**Results and discussion**

**(a) Divergent reactivity of $R_2E$ (R = $^t$Bu, Me; E = Se, S) with coinage metal reagents: Formation of ternary metal chalcogenide nanoparticles *via* a reactive Ag-Cu molecular intermediate Vs stable molecular complexes**

Direct reaction of $^t Bu_2Se$ with AgTFA and $Cu(TFA)_2$ (where TFA = trifluoroacetate) at room temperature resulted in gradual change in the color of the solution from blue to brown and finally precipitation of a black colored powder (Fig. S1). Warming the reaction mixture at 80 °C increased the yield. The powder XRD pattern of this black precipitate matched well with those of the previously published XRD results showing a mixture of two phases of ternary silver copper selenide, AgCuSe, i.e., PDF 010-0451 and 025-1180.[3-5] It also showed a small amount of $Ag_2Se$ NPs (PDF 01-080-7685, ~5% as quantified using reference intensity ratio (RIR) method (Fig. 1a). The SEM and TEM images show nanometric but somewhat irregular CuAgSe particles (Fig. 1b, S2 and S3), which is not surprising given that the synthesis was achieved in the absence of any capping ligand. The high resolution TEM (HRTEM) images clearly show an interplanar crystal lattice (Fig. 1c, S3). The fast Fourier transform (FFT) image shows the diffraction spots from the (1 0 0), (1 1 0), (1 1 1), (0 1 2), and (1 1 2) crystal planes (Fig. 1c inset). The absence of other elements apart from C, Cu, Ag, and Se in the Energy dispersive X-ray (EDX) analysis indicates the high purity of the nanoparticles (Fig. S4). The EDX analysis of several randomly selected area gives a slightly silver-rich stoichiometry due to presence of additional $Ag_2Se$ phase, as indicated by XRD. The NPs were further studied by the X-ray photoelectron spectroscopy (XPS) analysis, which shows that the nanoparticles are mainly composed of $Cu^+$, $Ag^+$ and $Se^{2-}$ with very small amounts of $Cu^{2+}$ and $Se^{4+}$, most probably due to the surface oxidation of nanoparticles (Fig. S5).[29] The Cu $2p_{3/2}$ state shows the presence of two electronic states located at 932.4 eV and 934 eV.[27] As the difference in the binding energy of $Cu^0$ and $Cu^+$ is very small

(only few meV), an Auger analysis was carried out by using the Auger parameter (AP).[30] In this case, AP is approximately 1850 attributable to $Cu^{+}$ for the first chemical state at 932.4 eV. The state located at 934 eV corresponds to $Cu^{2+}$ as further indicated by the presence of satellite sates around 943 eV. The spin orbit states for Ag $3d_{5/2}$ and $3d_{3/2}$, which appear at 368 and 374 eV, respectively, correspond to $Ag^{+}$.[28] The Se $3d_{5/2}$ state from $Se^{2-}$ appears at 53.6 eV.[27,28] The sate visible at 58.5 eV can be attributed to $Se^{4+}$.

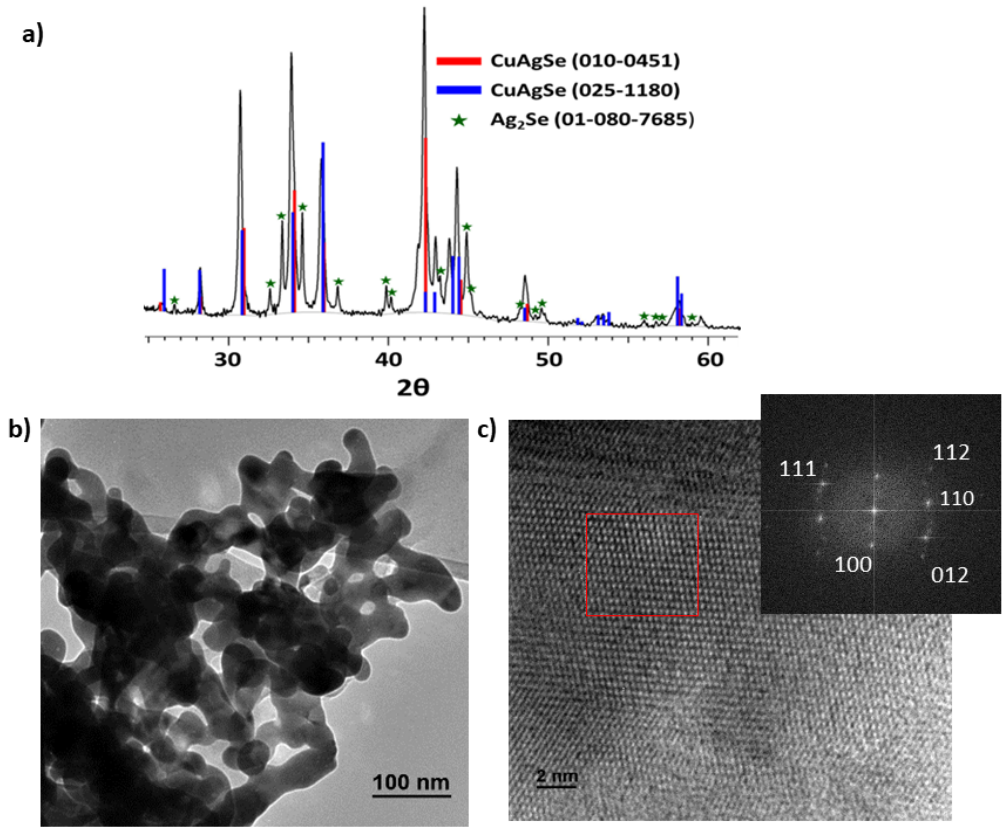


**Figure 1.** Characterization of AgCuSe NPs obtained at room temperature from the reaction of Ag(TFA), $Cu(TFA)_2$ and $^{t}Bu_2Se$. (a) XRD pattern, (b) TEM, (c) HR-TEM with FFT analysis given in inset.

Identification of reactive intermediate species operating at the interface of stable molecular complexes and nanoparticles is an important aspect and a key factor to (i) comprehand the mechanism of molecule-to-nanoparticle formation, and (ii) achieve a fine control over their chemical composition and reactivity to optimize the synthetic conditions and properties of the nanoparticles.[27,28] Therefore, attempts were made to identify the species present in the solution before the precipitation of AgCuSe NPs. We succeeded in isolating and characterising an intermediate molecular species $[Ag_2Cu(TFA)_4(^tBu_2Se)_4]$ **1** in good yield from the reactions mixture. Although **1** is highly reactive and turns black in few days even at low temperature and in inert atmosphere, apparently due to formation of metal selenide NPs, it is stable for sufficient duration to be characterized by single crystal X-ray, FT-IR, TG-DTA and thermochromic studies. The molecular structure of $[Ag_2Cu(TFA)_4(^tBu_2Se)_4]$ **1** is based on a spirocyclic metal–oxygen framework. It crystallizes in the orthorhombic space group *Pbca* and its structure can be conceptually seen as bidentate interaction of the two mono anionic $\{Ag(\mu\text{-}TFA)_2(^tBu_2Se)_2\}^-$ moieties with an electrophilic $Cu^{2+}$ center (Fig. 2a). The two six-membered boat-shaped 'AgO$_4$Cu' rings are fused at a common $Cu^{2+}$ centre. The tendency of the TFA to act as an assembling ligand to afford heterometallics has previously been highlighted.[31] Two terminal $^tBu_2Se$ ligands present on each of the silver atoms then complete a distorted tetrahedral $O_2Se_2$ environment around metal centers (if short Ag(I)•••Cu(II) interactions [3.589-3.679 Å] are not taken in to account), as revealed in the range of angles around the Ag center (93.72–131.21°). The Ag-O [2.412(6)-2.436(6) Å] and Ag-Se [2.581(1)-2.601(1) Å] bond lengths compare well with the literature values on the bridging trifluoroacetate and terminally bonded selenium-containing ligands, respectively.[27,28] The four oxygen atoms around Cu1 are essentially in the same plane and at almost same distance from the copper (Cu–O = 1.941(6)-1.944(6) Å].[32] These

trinuclear $Ag_2Cu$ species are discrete in nature with shortest intermolecular Ag…Ag interaction being 8.5 Å (Fig. 2b).

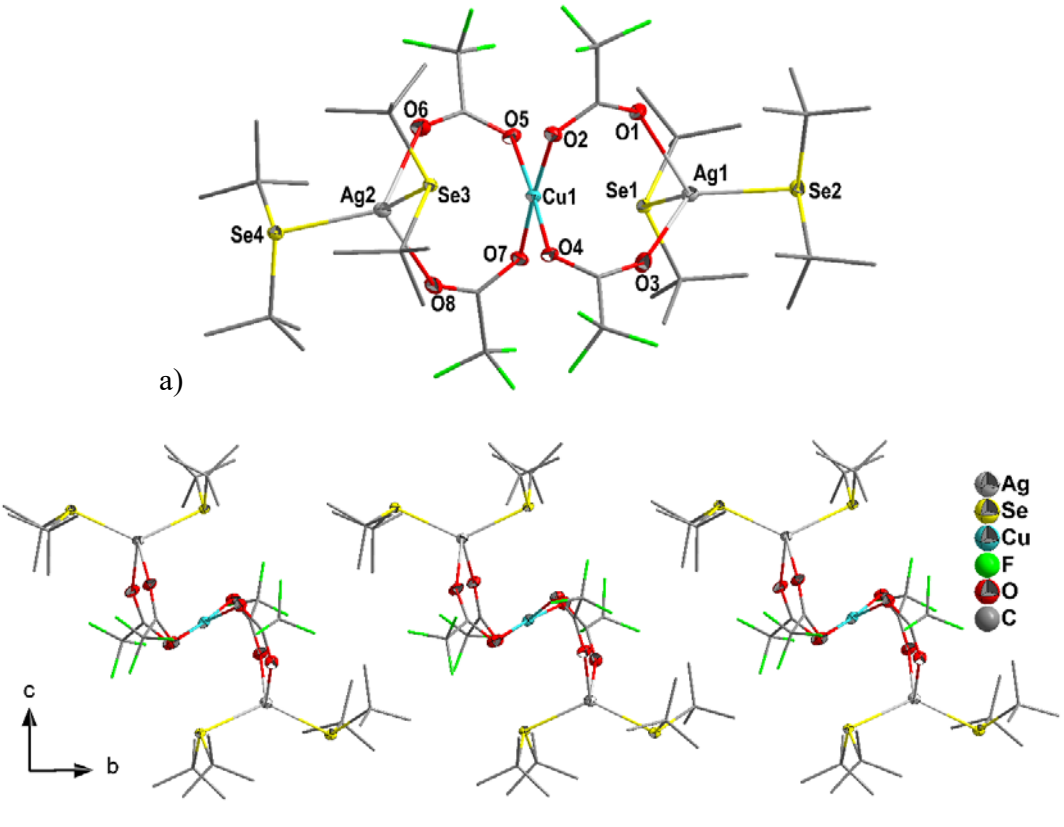


**Figure 2.** (a) Perspective view of the molecular structure of $[Ag_2Cu(TFA)_4(^tBu_2Se)_4]$ **1** with 50% probability ellipsoids (H atoms omitted for clarity). Selected bond lengths (Å) and angles (°): Ag2—O6 2.436(6), Ag2—O8 2.412(6), Cu1—O2 1.933(6), Cu1—O4 1.944(6), Ag1—Se2 2.581(1), Ag2—Se4 2.601(1), O1—Ag1—O3 93.7(2), Se1—Ag1—O1 102.1(2), Se2—Ag1—O1 109.9(1), Se1—Ag1—Se2 130.1(3), O2—Cu1—O5 87.4(3), O5—Cu1—O7 93.5(3). (b) Extended structure of **1** showing discrete nature of $Ag_2Cu$ trinuclear (shortest intermolecular Ag…Ag interaction being 8.5 Å).

The thermogravimetric studies of **1** confirmed its low thermal stability and high reactivity. The TG curve, recorded under $N_2$ atmosphere, indicates a 2-step decomposition in the temperature range 60–160 °C (Fig. 3a), with two DTG peaks at 82.5 and 91.5 °C. A residual mass of 27.9%

at 200 °C is consistent with the formation of 1 eq. AgCuSe + 0.5 eq. $Ag_2Se$ (calculated value 26.5%) as the end product. The high reactivity of **1** is further evident from the fact that it is transformed to a mixture of AgCuSe and $Ag_2Se$ on leaving in air for few hours (Fig. S6). It reacts differently with water and gives mainly $Ag_2Se$, $Cu_2Se$ and metallic silver (Fig. S7 and S8).

Similar reaction with $^tBu_2S$ in toluene did not lead to either change in color or any precipitation even after stirring for several hours at room temperature but yielded black precipitate immediately on refluxing. The XRD of this precipitate showed ternary silver copper sulfide $Ag_3CuS_2$ (PDF 04-016-6112) as the major phase, along with a small amount of $Ag_2S$ (PDF 00-068-0300) (Fig. S9). Blue colored crystals of the composition $[Ag_2Cu(TFA)_4(^tBu_2S)_4]$ (**2**) were readily obtained in good yield from the reactions mixture of Ag(TFA), $Cu(TFA)_2$ and $^tBu_2S$ at room temperature. In the FT-IR spectrum of **2**, the presence of only one strong band at 1715 $cm^{-1}$ due to $\nu_{as}CO_2$ (Fig. S10)[33,34] suggests a structure similar to **1** where TFA ligands show only one bonding mode. The structure of **2** is indeed similar to **1** and is given in the Fig. S11 in the supporting information. Unlike **1**, which turns gradually black even when kept in dark at low temperature and under inert atmosphere, complex **2** is stable at RT for several weeks. However, it decomposes in refluxing toluene to give a mixture of $Ag_3CuS_2$ (PDF 04-016-6112) and $Ag_2S$ (PDF 00-068-0300), the former being the major phase (Fig. 3c). This thermal instability can be explained by the thermogravimetric studies of **2** which indicates a single-step decomposition with only one DTG peaks at 120 °C (Figure 3b). The presence of a small amount of binary silver chalcogenide $Ag_2Se/Ag_2S$ in the ternary $AgCuSe/Ag_3CuS_2$ is not always a drawback and may actually be beneficial for certain applications. For example, we have recently shown that the presence of two phases of ternary metal chalcogenide in $AgCuSe-TiO_2$ composites enhances its photocatalytic activity due to synergic effect between them.[5]

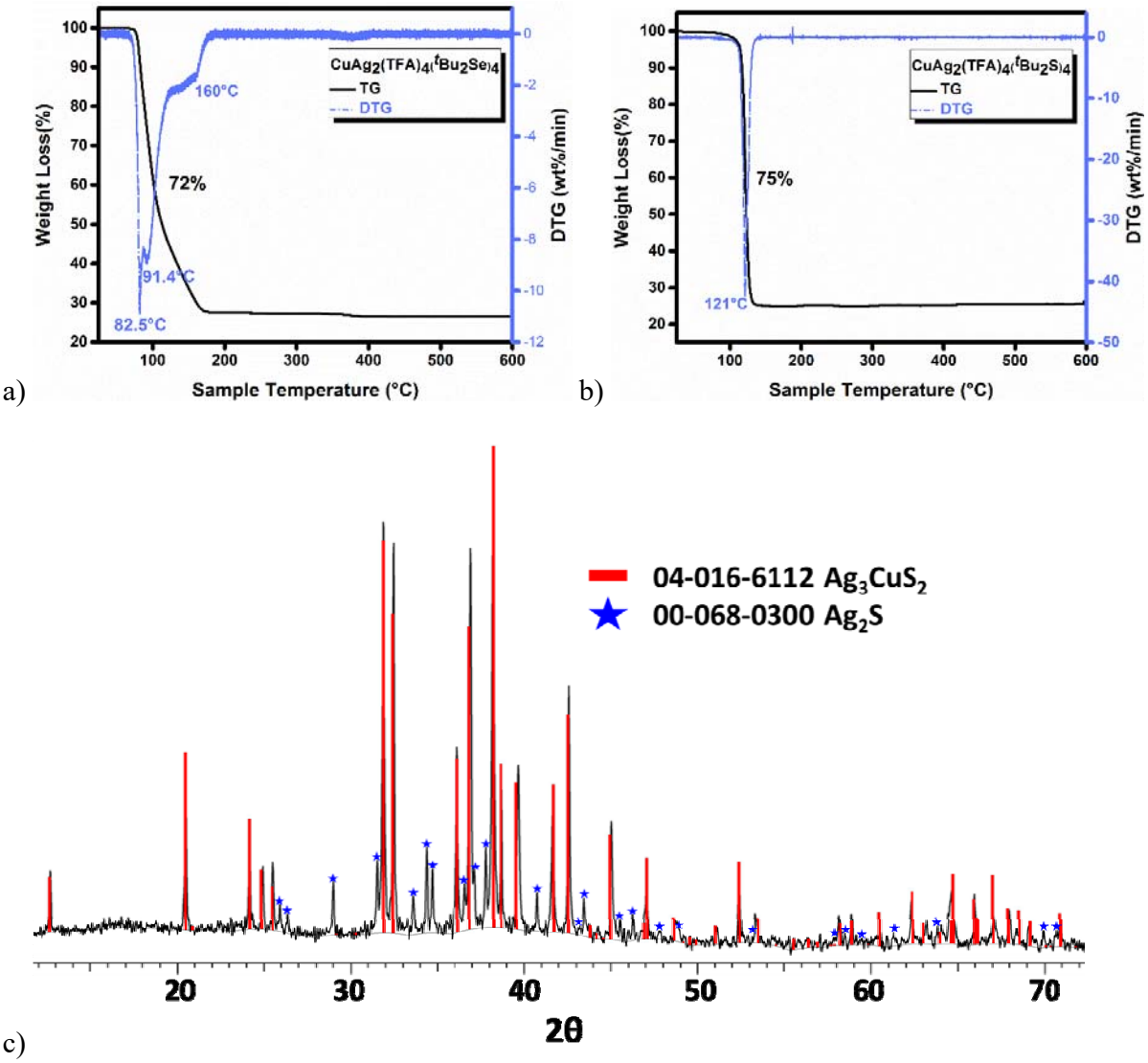


**Figure 3.** TG-DTG curves of **1** (a) and **2** (b). XRD pattern of the powder obtained after decomposition of **2** in refluxing toluene (c).

We then attempted to mimic the above reaction with the $Me_2E$ (E = Se, S) ligands, for which there is no possibility of decomposition *via* β-hydrogen elimination pathway.[27,28,35,36] As expected, these reactions yielded molecular complexes of similar composition $[Ag_2Cu(TFA)_4(Me_2E)_4]$ [E = Se (**3**), S (**4**)], which are kinetically as well as thermally stable**.** The isostructural **3** and **4** essentially have a structure that is similar to their $^tBu_2E$ (E = Se, S) analogues **1** and **2** at trinuclear level (Fig. 4, S13). However, unlike discrete nature of the

trinuclear $Ag_2Cu$ units in **1** and **2**, these units have strong Ag•••Ag interaction (2.5-3.23 Å) in **3** and **4** to give 1D chain. As a result, the Ag-O bond lengths are slightly longer here [2.438(7)-2.528(6) Å in **4** vs 2.391(4)-2.436(6) in **1** and **2**]. The four oxygen atoms around Cu1 are arranged in the same plane with Cu–O distances [1.932(6)-1.946(5) Å] being comparable to those found in **1** and **2**. The Ag-S distances are spread in the range 2.458(2)-2.486(2) Å. The polymeric nature of **3** and **4** is reflected in their TG-DTG curves which show multi-step thermal decomposition that lasts well beyond 300 °C (Fig. S14). On decomposition under inert atmosphere at 350 °C, **3** is transformed to a mixture of AgCuSe and $Ag_2Se$ (and a very small impurity of the metallic Ag) (Fig. S15).

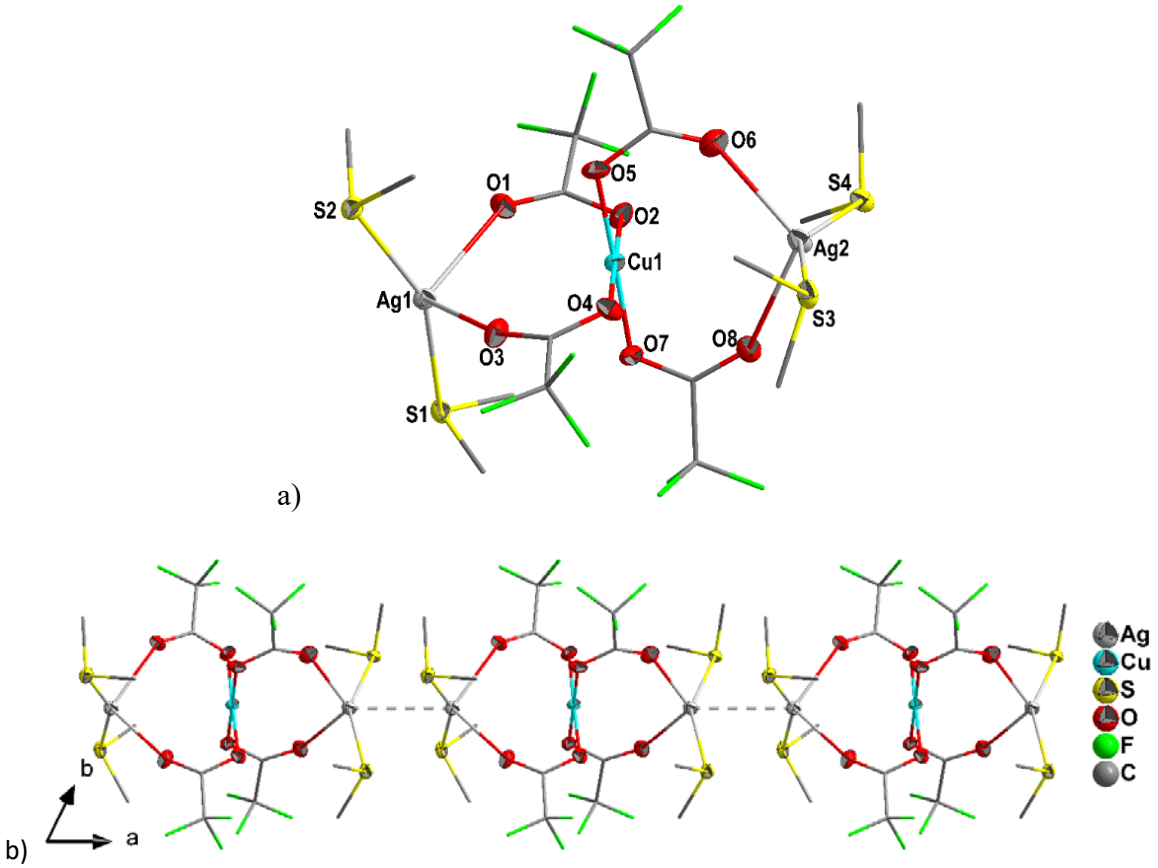


**Figure 4.** (a) Perspective view of the molecular structure of $[Ag_2Cu(TFA)_4(Me_2S)_4]$ **4** with 50% probability ellipsoids (H atoms omitted for clarity). (b) Extended structure with short Ag…Ag

interaction (3.23 Å) among $Ag_2Cu$ trinuclear units to afford 1 D chain. Selected bond lengths (Å) and angles (°): Ag1—S1 2.458(2), Ag1—S2 2.476(2), Ag1—O1 2.511(6), Ag1—O3 2.528(6), Ag2—S4 2.486(2), Ag2—S3 2.461(2), Ag2—O8 2.501(7), Ag2—O6 2.438(7), Cu1—O2 1.933(5), Cu1—O4 1.946(5), Cu1—O7 1.932(6), Cu1—O5 1.934(6), S1—Ag1—S2 153.63(7), S1—Ag1—O1 107.61(18), S1—Ag1—O3 97.38(16), S2—Ag1—O1 92.93(17), S2—Ag1—O3 94.14(15), O1—Ag1—O3 102.1(2), S4—Ag2—O8 92.99(15), S3—Ag2—S4 148.58(7), S3—Ag2—O8 95.82(15), O6—Ag2—S4 95.93(19), O6—Ag2—S3 108.6(2), O6—Ag2—O8 111.6(3), O2—Cu1—O4 179.2(2), O2—Cu1—O5 88.7(2), O7—Cu1—O2 92.1(2), O7—Cu1—O4 87.9(2), O7—Cu1—O5 178.6(2), O5—Cu1—O4 91.3(2).

Silylated chalcogenoethers $(Me_3Si)_2E$ (E = S, Se, Te) are important reagents for the solution phase synthesis of metal chalcogenides under mild conditions.[16] However, their mechanism has been subject of many speculation. Formation of a sulfide-bridged intermediate $[(NHC)_2Ag_2(\mu\text{-}S)]$ (NHC = N-heterocyclic carbene) has been suggested during the formation of $Ag_2S$ NPs from the room temperature reaction of $(Me_3Si)_2S$ with (NHC)AgX (X = a halide), though no structural evidence was presented.[37] On the other hand, the reaction of $(Me_3Si)_2E$ with the related (NHC)Cu(OAc) was shown to afford thermally stable complexes $[(NHC)Cu–ESiMe_3]$ (E = S, Se, Te) at low temperature,[38] suggesting the conversion of chalcogenoethers to chalcogenolates before affording metal chalcogenide NPs. Using bulkier non-silylated dialkylselenide $^tBu_2Se$, which is slightly less reactive than its silylated counterpart but still gives metal selenide NPs with group 11 metal reagents at room temperature, we have been able to isolate reactive intermediates $[Cu_2(TFA)_2(^tBu_2Se)_3]$ and $[Ag(TFA)(^tBu_2Se)_2]$ that confirmed that $Cu_{2-x}Se$ and $Ag_2Se$ NPs are formed *via* these intermediates.[27,28] The synthesis of ternary metal chalcogenide materials is even more challenging and there are very few single source precursors (SSPs) reported so far for

them. The heterometallics $[Ag_2Cu(TFA)_4(R_2E)_4]$ (R = Me, $^t$Bu; E = S, Se) described here not only fill this clear void of SSPs for such ternary chalcogenide materials, but more importantly, some of them were isolated as highly reactive intermediates, which can provide tailored reactivity for investigating the fundamentals of nucleation and growth of these ternary materials.

The high reactivity of $^t$Bu$_2$E (E = Se, S) to give metal chalcogenide nanoparticles under mild conditions can be attributed to availability of a decomposition path *via* β-hydrogen elimination, which first leads to formation of *tert*-butylchalcogenol and then chalcogenide ligand (Eqn. S1-S3).[39] This mechanism finds support from the above mentioned isolation of chalcogenolate complexes [(NHC)Cu–ESiMe$_3$] (E = S, Se, Te) and proposed sulfide-bridged intermediate [(NHC)$_2$Ag$_2$(μ-S)] during the reaction of (Me$_3$Si)$_2$S with (NHC)Cu(OAc) and (NHC)AgX, respectively.[37,38] Higher reactivity of selenide precursors in comparison to analogous sulfide precursors has previously been demonstrated and explained on the basis of DFT calculations.[12] The coordinated $^t$Bu$_2$E (E = Se, S) ligands play a dual role in the formation of metal chalcogenide NPs *i.e.,* a facile source of chalcogens and a reducing reagent to get desirable +1 oxidation state of the copper center.

**(b) DFT calculations**

DFT calculations were performed on $[CuAg_2(TFA)_4(R_2E)_4]$ [R = $^t$Bu, E = Se (**1**), S (**2**); R = Me, E = Se (**3**), S (**4**)] to gain information about their electronic structures and, consequently, their reactivity and properties. Popular quantum mechanical descriptors e. g, the HOMO-LUMO energies play a major role in governing wide range of chemical interactions. The Frontier Molecular Orbital gives an insight about the reactivity of the molecule and the active site can be demonstrated by the distribution of frontier orbital. The HOMO-LUMO energy gap generally

implies the kinetic energies and chemical reactivity rate. The energy gap between the highest occupied molecular orbital (HOMO) and the lowest unoccupied molecular orbital (LUMO) electronic levels is a critical parameter that corresponds to the energy difference between the ionization potential and electron affinity of a molecular species or material and determines its electronic, optical, redox, and transport (electrical) properties. The band gap is also referred to as the transport gap since it represents the minimum energy necessary to create a positive charge carrier somewhere in the material minus the energy gained by adding a negative charge carrier. The HOMO and LUMO energies as well as the HOMO-LUMO energy gaps of **1**-**4** are presented in Table 1. The HOMO-LUMO gap of 0.25, 3.13, 2.09, and 3.06 eV are calculated for **1**-**4**, respectively, which confirm the kinetic instability and higher chemical reactivity of **1**. This is further confirmed by the temperature dependent simulation of **1**-**4** at 353 and 393 K, performed for 200 ps with a timestep of 1 fs (Supplementary video S1). Fig. S16 gives some intrinsic insights to the structural properties and stabilities of **1**-**4** simulated under constant pressure and varying temperatures. As compared to the **2**-**4**, the reactive intermediate **1** shows the highest fluctuation in total energy difference ΔE variation and takes highest steps to reach the equilibrium (Fig. 5 and 6). The Langevin thermostat & production with Nose-Hoover (NVT) ensemble for 200 ps for **1**-**4**, where number of atoms (N), volume (V) and temperature (T) were kept constant, represents the stability of the structures as a function of total energy (Fig. 7). The high total energy variation can only be observed for the **1** both at 353 and 393 K, which is in accordance with its structural deformation as depicted previously in the Figure S16. The isothermal and isobaric (NPT) ensemble for 200 ps as a function of total energy for **1**-**4** at 353 and 393 K temperature, where number of atoms (N), pressure (P) and temperature (T) were conserved, are depicted in the Figure S17. The observed large volumetric expansion for the **1** at

353 K and less expansion of volume at 393 K indicates its instability at 353 K as compared to the **2**-**4**. Figure S18 shows the pair distribution function g(r) that accounts for the number of neighbors for each atom that are within a given cut-off range (in our case at r = 3.5) around its position by analyzing the structural stability at different temperatures. The RDF $g(r)$ measures the probability of finding a particle at distance $r$ given that there is a particle at position 0; it is essentially a histogram of inter-particle distances. The pair distribution function is normalized by the number density of particles (i.e. total number of particles divided by the simulation cell volume).

**Table 1.** The HOMO and LUMO energies and the HOMO-LUMO band-gap for **1**-**4**.

| **Molecular species** | **HOMO** | **LUMO** | **ΔE** |
|---|---|---|---|
| **$CuAg_2(TFA)_4(^tBu_2Se)_4$ (1)** | -3.68176 | -3.43226 | 0.25 |
| **$CuAg_2(TFA)_4(^tBu_2S)_4$ (2)** | -0.15735 | 2.9695 | 3.13 |
| **$CuAg_2(TFA)_4(Me_2Se)_4$ (3)** | -0.43356 | 1.659036 | 2.09 |
| **$CuAg_2(TFA)_4(Me_2S)_4$ (4)** | -0.63741 | 2.42129 | 3.06 |

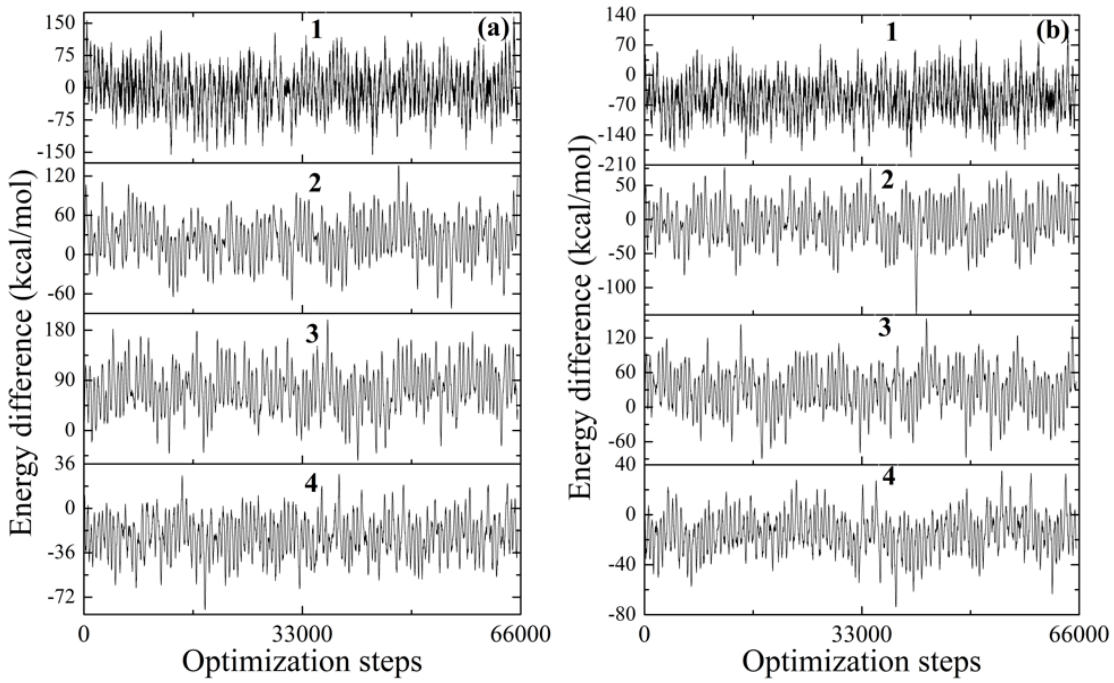


**Figure 5.** The fluctuation in energy of system as a function of optimization steps for **1**-**4** at 353 (a) and 393 K (b) [molecular dynamics (MD) simulations].

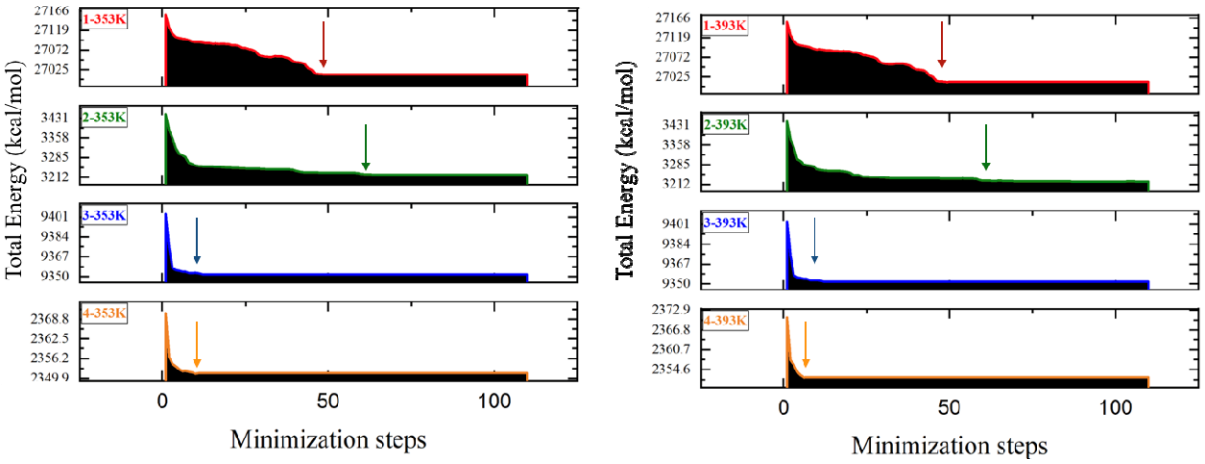


**Figure 6.** The steps of optimized structures as a function of total energy for **1**-**4** at 353 and 393 K.

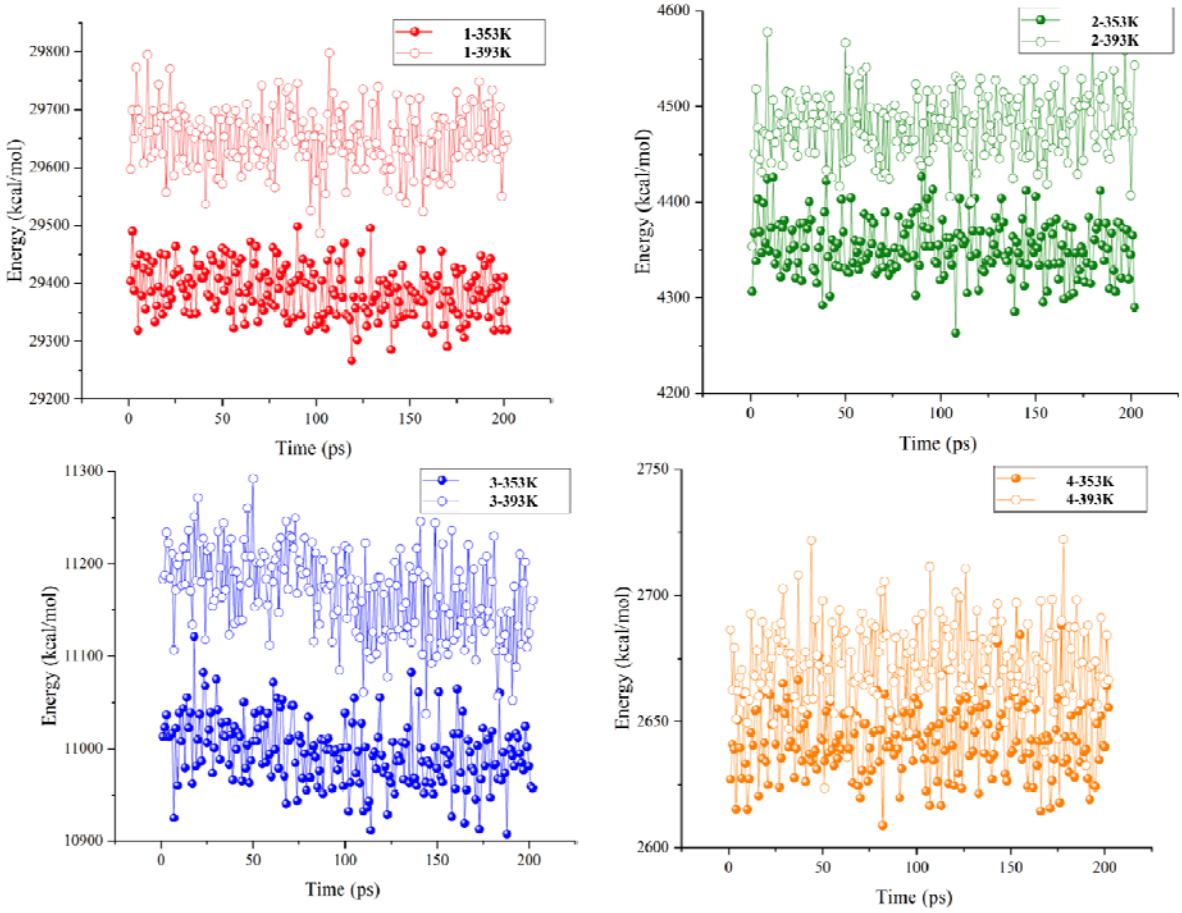


**Figure 7.** The Langevin thermostat & production with Nose-Hoover (NVT) ensemble for 200 ps as a function of total energy for **1**-**4** at 353 and 393 K.

**(c) Thermochromic behavior of 1**

Interestingly, when taken in a coordinating solvent (or even in the contact with the vapor of this solvent), the color of **1** changes from blue (273 K and below) to green at room temperature (Fig. 8 inset, Fig. S19, video S2 in supplementary information). Figure 8 shows the evolution of the peaks at 463 nm (blue) and 543 nm (green) in the absorption spectrum of **1** in THF in terms of blue to green (B/G) ratio as a function of the temperature. As temperature increases, the B/G ratio continuously decreases till the complex decomposes at about 330 K. The simulated UV-

visible absorption spectra of **1**-**4** at room temperature are presented in Figure S20. While **1** has relatively higher intensity of the absorption bands and shows the most dominating peak at around 550 nm, the compounds **2**-**4** have the most dominant absorption bands in the region 430-460 nm. As expected, the absorption spectrum of the kinetically and thermally instable **1** shows significant changes at 353 K whereas **4,** which is thermally stable, presents similar absorption peaks at high temperature (although of slightly different intensity) (Fig. 9).

As **1** is not thermochromic in non-coordinating solvent such as toluene (Fig. S21), it is very probable that the above reversible phenomenon is due to coordination/dis-coordination of the THF molecule with the copper atom. In the X-ray structure of **1** at 100 K, the copper center has weak intramolecular interactions with Ag (3.59-3.68 Å) and Se atoms (3.87-3.95 Å). At room temperature, these interactions are expected to further weaken, thus allowing solvent THF molecules to get weakly coordinated with copper center, which would, by virtue of dynamic Pseudo Jahn-Teller effect, cause red shift in the absorption (blue to green).[40-42] This theory is further supported by the fact the complex **2**, which has stronger Cu…S interaction (3.55 Å), or **3** and **4** which are structurally more rigid due to additional intermolecular Ag…Ag interaction (2.5-3.23 Å) among $Ag_2Cu$ trinuclear units, do not demonstrate any visible thermochromism and the B/G ratio does not change significantly with temperature (Fig. 8, video S3 in supplementary information). Unfortunately, our efforts to corroborate further above theory by measuring the single crystal X-ray structure of **1** at room temperature were not successful due to instability of this compound which decomposed after few frames of data collections.

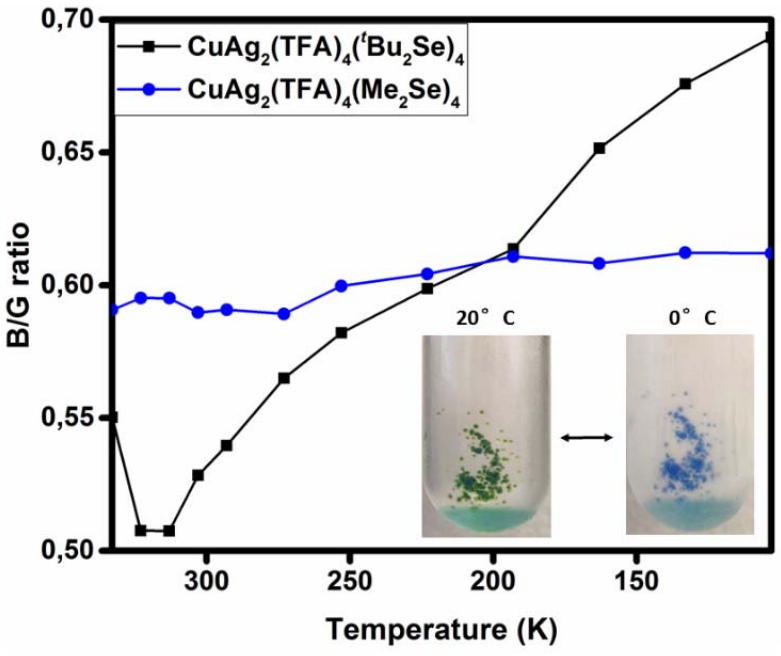


**Figure 8.** Change in the absorption intensity of blue (463 nm) and green (543 nm) peaks of **1** and **3** taken in THF, in terms of blue to green (B/G) ratio, as a function of the temperature. The photos at the bottom show two different colors of **1** at two different temperatures.

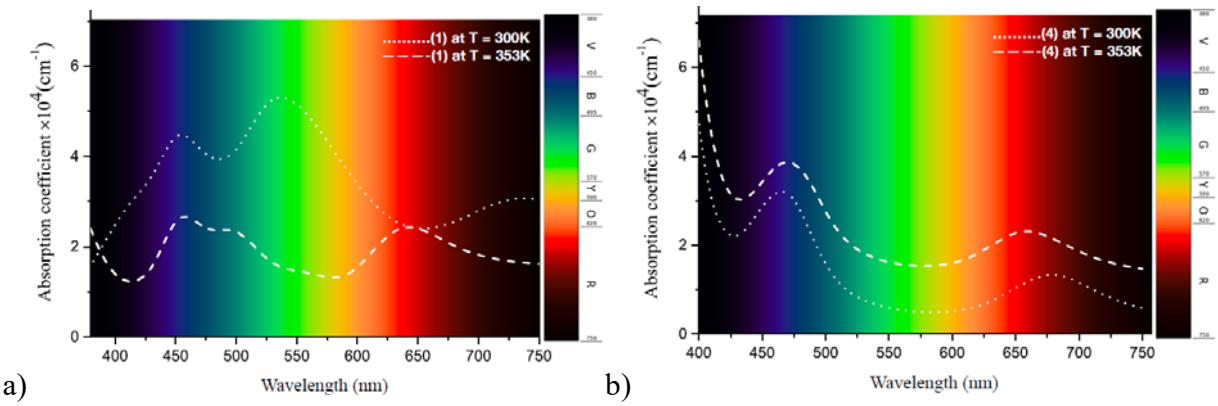


a) b)

**Figure 9.** The simulated UV-visible absorption spectra of **1** (a) and **4** (b) at variable temperature.

## Conclusions

Mild synthesis of ternary coinage metal chalcogenides AgCuSe and $Ag_3CuS_2$ from the reaction of Ag(TFA) and $Cu(TFA)_2$ with $^tBu_2Se$ or $^tBu_2S$ are presented. Successful isolation and characterization of intermediate species during the course of these reactions,

$[Ag_2Cu(TFA)_4(^tBu_2E)_4]$ [E = Se (**1**), S (**2**)], establishes a precursor-mediated pathway for the formation of ternary metal chalcogenides. The highly reactive intermediate $[Ag_2Cu(TFA)_4(^tBu_2Se)_4]$ **1** is thermally and kinetically instable, as confirmed by the thermogravimetric studies and the DFT calculations, and shows an interesting thermochromic behavior (green at 20 °C and blue at RT). In contrast, the analogue complexes with $^tBu_2S$ and $Me_2E$ ligands i.e., $[CuAg_2(TFA)_4(R_2E)_4]$ [R = $^t$Bu, E = S (**2**); R = Me, E = Se (**3**), S (**4**)] are kinetically stable and non-thermochromic in nature. In addition to the utility of these heterometallic precursors in the solution-phase synthesis of ternary metal chalcogenide NPs, their tailored reactivity can also be used to study the fundamentals of nucleation and growth of ternary materials.

## Experimental

**General Procedures.** We performed all the manipulations under an argon atmosphere using standard Schlenk and glovebox techniques. Solvents were dried using MB SPS-800 and used without further purification. Silver trifluoroacetate (Aldrich), di-*tertiary*-butyl selenide (SAFC Hitech), di-*tert*-butyl sulfide and di-methyl sulfide (TCI Europe N.V.), dimethyl selenide and copper(II) trifluoroacetate hydrate (Alfa Aesar) were purchased and used without further purification, whereas copper(II) trifluoroacetate tetrahydrofuran adduct was synthesized in the laboratory from the reaction of $Cu_2O$ and TFAH in THF. The infrared spectra were obtained as Nujol mulls on a Bruker Vector 22 FT-IR spectrometer at room temperature and registered from 4000 to 400 $cm^{-1}$. Scanning electron microscopy (SEM) measurements were performed on a Hitachi S800 system. TEM experiments were performed using a JEM-2100F system with 200 kV field emission (FE) and a JEOL 2010 $LaB_6$ system with 200 kV FE. We used a Bruker D8

Advance A25 system with Cu Kα1 + 2 (λ = 0.154184 nm) radiation at 50 kV and 35 mA to measure the X-ray diffraction (XRD) patterns of the powdered crystals. Cu, Ag, S and Se contents were determined by inductively coupled plasma-optical emission spectroscopy (ICP-OES). Thermogravimetric analyses (TGA) were performed with a TGA/DSC 1 STARe System from Mettler Toledo. Around 8 mg of the samples were sealed in a 100 µl Al crucibles in the glovebox and heated under argon atmosphere at a heating rate of 5 °C/min. The diffusion-reflectance measurements were performed on a homemade apparatus. The sample was illuminated by an EQ99X laser-driven point source of the lamp and it was reimaged on the sample by two 100 m focal length, 2 inch diameter $MgF_2$ lenses. The emitted light from the sample was collected by an optical fiber connected to a Jobin-Yvon TRIAX320 monochromator equipped with a cooled CCD detector. The resolution of the detection system was 2 nm. For the temperature variation, the sample was placed on a cooling stage from LINKAM ltd. DSC600 which allowed to vary the temperature from liquid nitrogen.

**Synthesis of CuAgSe nanoparticles and isolation of Ag-Cu heterometallic molecular intermediate**. A reaction mixture of $Cu(TFA)_2(THF)$ (0.05 g, 0.14 mmol), Ag(TFA) (0.03 g, 0.14 mmol) and $^tBu_2Se$ (0.1 mL, 0.56 mmol) was stirred in the absence of any solvent at room temperature, which led to gradual change in the color of the solution from blue to brown and finally a black colored powder was precipitated. After stirring the reaction mixture for 1.5 h, the black precipitate was isolated, washed with ethanol several times and dried at room temperature. The powder XRD of this black precipitate confirmed it to be CuAgSe nanoparticles containing also ~5% of $Ag_2Se$ nanoparticles.

We then made attempts to isolate intermediate molecular species present in the solution during the course of above reaction. We carried out above reaction under varied conditions (different reaction time and solvents such as toluene, THF, diethylether…) in order to avoid the black precipitation and to isolate molecular species. In one such optimized reaction, 0.20 mL of $^{t}Bu_2Se$ (1.10 mmol) was added to a blue colored toluene solution (20 mL) containing $Cu(TFA)_2(THF)$ (0.1 g, 0.28 mmol) and Ag(TFA) (0.06 g, 0.28 mmol) and the resulting solution was stirred for 15 min at room temperature. After that the solution was concentrated under vacuum and layered with *n*-pentane (10 mL) to obtain dark blue crystals of **$[CuAg_2(TFA)_4(^{t}Bu_2Se)_4]$ (1)** along with few colorless crystals of the composition $[Cu_2(TFA)_2(^{t}Bu_2Se)_3]$ **(a)**. The mother liquor was separated through a cannula and concentrated to give more amount of the compound **(a)**. The formation of compound **(a)**, which was previously reported by us,[27] can be explained by the fact that only half of the $Cu(TFA)_2$ is consumed during the formation of the heterometallic **1** which has 2:1 ratio of the Ag and Cu atoms. The blue crystals of **1** were isolated and washed with cold *n*-pentane. Yield, 0.17 g (52%). FT-IR (Nujol, $cm^{-1}$): 1712s, 1460s,1381s, 1200m, 1139m, 729m, 842w, 793w, 525w.

Alternatively, the compound **1** can also be synthesized in a better yield and without having any contamination of the copper species (**a**) by reacting $[CuAg_2(TFA)_4(Me_2Se)_4]$ **(3)** (please see below for the synthetic details of **3**) with $^{t}Bu_2Se$ in toluene. In this reaction, $^{t}Bu_2Se$ (0.07 mL, 0.37 mmol) was dropwise added to a solution of $[CuAg_2(TFA)_4(Me_2Se)_4]$ (**3**) (0.11 g, 0.09 mmol) in toluene (3 mL) which led to a change in the color of the solution from blue to green (Fig. S22). This mixture was stirred at room temperature for 20 minutes and then layered with *n*-pentane (7 mL). On diffusion, it gave a blue-colored solution from which blue crystals of $[CuAg_2(TFA)_4(^{t}Bu_2Se)_4]$ (**1**) were obtained at 0 °C. The mother liquor was removed through a

cannula, and the crystals were washed with cold *n*-pentane. Yield, 0.08 g (71%). **1** is highly reactive and instable, and turns black in 1-2 days even when kept at low temperature and under inert atmosphere. This precluded us to perform its elemental analysis. FT-IR (Nujol, $cm^{-1}$): 1714s, 1463s,1382s, 1205m, 1144m, 733m, 845w, 798w, 526w.

**Synthesis of $Ag_3CuS_2$ nanoparticles and isolation of Ag-Cu heterometallic molecular intermediate.** In contrast to above reaction, the reaction of $Cu(TFA)_2(H_2O)$ (0.3 g, 0.96 mmol), Ag(TFA) (0.21 g, 0.96 mmol) and $^tBu_2S$ (0.85 mL, 4.80 mmol) in toluene (30 mL) did not lead to any change in the colour at room temperature. However, under reflux, the color of the solution changed from dark blue to dark green and and after some time, black coloured powder was precipitated. After 3 hrs of refluxing, the precipitates were collected and washed thoroughly with ethanol and then dried at room temperature. The final product, when characterized by powder XRD technique, was found to be a mixture of $Ag_3CuS_2$ (70%) and $Ag_2S$ (30%). Yield, 0.09 g (42% wrt Ag).

As the reaction medium was stable at room temperature, attempt to isolate intermediate molecular species present in the solution during the course of above reaction was relatively straightforward. The green colored toluene solution (30 mL) containing $Cu(TFA)_2(H_2O)$ (0.32 g, 1 mmol), Ag(TFA) (0.22 g, 1 mmol) and $^tBu_2S$ (0.7 mL, 4 mmol), after stirring for 1 h, was concentrated and layered with *n*-hexane to obtain dark blue crystals of $[CuAg_2(TFA)_4(^tBu_2S)_4]$ (**2**) along with few green crystals later identified as $[Cu(TFA)_2(^tBu_2S)]$ (**b**) by the elemental analysis. The formation of compound **(b)** can be explained by the fact that only half of the $Cu(TFA)_2$ is consumed during the formation of the heterometallic **2** which has 2:1 ratio of the Ag and Cu atoms. The blue crystals of **2** were isolated and washed with cold *n*-pentane. Yield, 0.58

g (62 %). FT-IR (Nujol, cm-1): 1694s, 1465s, 1367s, 1200s, 842m, 790m, 724m, 668w, 615w, 592w, 522w. The reaction in the right stoichiometry [$Cu(TFA)_2(H_2O)$] (0.2 g, 0.64 mmol), Ag(TFA) (0.28 g, 1.29 mmol) and $^tBu_2S$ (0.46 mL, 2.58 mol)] improved the yield of the product (78%) and avoided the contamination of the copper species (**b**). Calc. for $C_{40}H_{72}Ag_2CuF_{12}O_8S_4$ (1316.5): C, 36.46; H, 5.47; Ag, 16.38; Cu, 4.83; S, 9.74. Found: C, 36.21; H, 5.29; Ag, 16.23; Cu, 4.73; S, 9.65. FT-IR (Nujol, $cm^{-1}$): 1694s, 1465s, 1367s, 1200s, 842m, 790m, 724m, 668w, 615w, 592w, 522w. Unlike **1,** the **2** is stable for several days when kept at low temperature/ room temperature and under inert atmosphere.

**Synthesis of stable $[CuAg_2(TFA)_4(Me_2Se)_4]$ (E = Se, S)**

**$[CuAg_2(TFA)_4(Me_2Se)_4]$ (3).** After the dropwise addition of $Me_2Se$ (0.1 mL, 1.30 mmol) to a blue colored solution of $Cu(TFA)_2(THF)$ (0.1 g, 0.28 mmol) and Ag(TFA) (0.12 g, 0.54 mmol) in THF (20 mL), the resulting solution was stirred for 2 hours at room temperature. After concentrating the solution, it was layered with *n*-hexane (10 mL) to obtain dark blue crystals of **3**. Mother liquor was removed through a cannula and the crystals were isolated and washed with cold *n*-pentane. Yield, 0.19 g (56%). Calc. for $C_{16}H_{24}Ag_2CuF_{12}O_8Se_4$ (1167.5): C, 16.44; H, 2.06; Ag, 18.48; Cu, 5.44; Se, 27.06. Found: C, 16.40; H, 1.98; Ag, 18.45; Cu, 5.40; Se, 26.90. FT-IR (Nujol, $cm^{-1}$): 1715s,1456s, 1377s, 725s, 970m, 928m, 846m, 793m, 521m, 601w, 427w.

Using above method, the compound $[CuAg_2(TFA)_4(Me_2S)_4]$ (**4**) was synthesized from $Cu(TFA)_2(H_2O)$ (0.10 g, 0.32 mmol), Ag(TFA) (0.14 g, 0.64 mmol) and $Me_2S$ (0.1 mL, 1.47 mmol) in $Et_2O$ (30 mL) and crystallized as dark-blue crystals by layering the concentrated solution with *n*-hexane. Yield, 0.22 g (68%). Calc. for $C_{16}H_{24}Ag_2CuF_{12}O_8S_4$ (979.87): C, 19.60; H, 2.45; Ag, 22.02; Cu, 6.48; S, 13.09. Found: C, 19.43; H, 2.34; Ag, 21.79; Cu, 6.43; S, 12.89.

FT-IR (Nujol, $cm^{-1}$): 1682s, 1457s, 1377s, 1198s, 1151s, 726s, 1036m, 987m, 843m, 792m, 679w, 668w, 606w, 523w.

**Decomposition of $[CuAg_2(TFA)_4(^tBu_2Se)_4]$ (1) in air.** On exposing to air, the crystals of **1** (0.05 g) turned black in few hours. The powder XRD on these black crystals after 3 days showed the presence of CuAgSe and $Ag_2Se$ phases in approximately equal proportions (Fig. S6).

**Hydrolysis of $[CuAg_2(TFA)_4(^tBu_2Se)_4]$ (1).** Reaction of water (0.5 mL) with **1** (0.05 g taken in 5 mL toluene) at an ambient atmosphere resulted in a light grey solution within the first few minutes, which on further stirring for 3 h, gave black colored precipitates consisting mainly of $Cu_2Se$, $Ag_2Se$ and metallic Ag, as revealed by powder XRD (Fig. S7 and S8).

**Thermal Decomposition of $[CuAg_2(TFA)_4(^tBu_2S)_4]$ (2).** 0.14 g dark blue crystals of **2** were dissolved in toluene (30 mL). After adding 0.5 mL of $^tBu_2S$, the solution was refluxed for 1 hour to obtain black precipitates. Powder XRD results of this sample confirmed the presence of $Ag_3CuS_2$ as major phase along with $Ag_2S$ (Fig. 3).

**Thermal decomposition of $[CuAg_2(TFA)_4(Me_2Se)_4]$ (3).** 0.15 g of **3** was decomposed in solid state at 350 °C for 2 hours in an inert atmosphere to obtain a black colored precipitates, the powder XRD of which showed the presence of CuAgSe as the major phase along with a small amounts of $Ag_2Se$ and metallic Ag (Fig. S15).

**X-ray crystallography:** Crystals of **1-4** were obtained as described in the synthetic procedure. Crystal structures were determined using Mo radiation (λ = 0.71073 Å) on an Oxford Diffraction Gemini diffractometer equipped with an Atlas CCD detector. Intensities were collected at 100 K by means of CrysAlisPro software.[43] Reflection indexing, unit-cell parameter refinement, Lorentz-polarization correction, peak integration and background determination were carried out with CrysAlisPro software.[43] An analytical absorption correction was applied using the modeled faces of the crystal.[44] The resulting sets of hkl were used for structure solutions and refinements. The structures were solved with the ShelXT[45] structure solution program using intrinsic phasing and by using Olex2[46] as the graphical interface The model was refined with version 2018/3 of ShelXL[47] using least squares minimization. Some selected crystallographic and refinement data of **1**-**4** are listed in Table 2.

Table 2. Crystallographic and refinement data for **1**-**4**.

| Compound | **1** | **2** | **3** | **4** |
|---|---|---|---|---|
| Empirical formula | $C_{40}H_{72}Ag_2CuF_{12}O_8Se_4$ | $C_{40}H_{72}Ag_2CuF_{12}O_8S_4$ | $C_{48}H_{72}Ag_6Cu_3F_{36}O_{24}Se_{12}$ | $C_{16}H_{24}Ag_2CuF_{12}O_8S_4$ |
| Formula weight | 1504.1 | 1316.5 | 3502.4 | 979.9 |
| Crystal system | Orthorhombic | Monoclinic | Monoclinic | Triclinic |
| Space group | *Pbca* | *C2/c* | *P2₁/n* | *P*-1 |
| a (Å) | 17.9685(15) | 17.4632(11) | 17.0247(11) | 10.4336(10) |
| b (Å) | 22.642(4) | 16.5079(9) | 31.466(3) | 11.0465(9) |
| c (Å) | 27.703(3) | 20.0811(14) | 19.6823(19) | 16.3292(10) |
| α (°) | 90 | 90 | 90 | 75.224(6) |
| β (°) | 90 | 101.451(7) | 104.751(8) | 86.689(6) |
| γ (°) | 90 | 90 | 90 | 64.143(9) |
| V (Å$^3$) | 11270(2) | 5673.8(6) | 10196.4(15) | 1634.5(3) |
| Z | 8 | 4 | 4 | 2 |
| μ (mm$^{-1}$) | 3.73 | 1.28 | 6.15 | 2.19 |
| Temperature (K) | 100 | 150 | 150 | 150 |

| | | | | |
|---|---|---|---|---|
| Measured reflections | 48269 | 38823 | 79599 | 14879 |
| Independent / observed [I > 2σ(I)] reflections | 13493/7579 | 7289/5967 | 24441/13442 | 14879/9923 |
| $R_{int}$ | 0.086 | 0.041 | 0.096 | 0.09 |
| Restrains / parameters | 69/656 | 533/428 | 1080/1150 | 0/396 |
| Goodness of fit | 1.03 | 1.10 | 1.61 | 1.07 |
| $R[F^2 > 2\sigma(F^2)]$ | 0.069 | 0.046 | 0.180 | 0.071 |
| $wR(F^2)$ | 0.204 | 0.119 | 0.507 | 0.224 |
| Residual electron density (e $Å^{-3}$) | -1.67 to 2.55 | -1.07 to 0.68 | -3.24 to 13.92 | −1.53 to 3.47 |
| CCDC no. | 1903337 | 1968807 | 1903338 | 1968808 |

**Computational details:** In the present work, we have performed the electronic structure calculations within density functional theory (DFT)[48,49] which is implemented in the Vienna Ab-initio Simulation Package (VASP) code.[50] The projector augmented wave (PAW) potentials were adopted to describe between cores and valence electrons.[51] The generalized gradient approximation (GGA) functional in the form of Perdew, Burke and Ernzerhof (PBE) were adopted to describe the exchange and correlation potentials.[52] We have chosen k-point sampling (5x4x3), (5x5x5), (5x2x5) and (7x7x5) for **1**-**4**, respectively, for Brillouin Zone (BZ) integration in k-space. Here, the k-point mesh is generated by Monkhorst-Pack scheme.[53] The kinetic energy cut-off for plane wave basis set is 600 eV. Atoms are optimized until the force per atom in unit cell was converged within $10^{-3}$ eV/Å. The energy convergence criterion for per self-consistent is $1\times10^{-6}$ eV. For simplistic visualization of the structural configurations at various temperatures e.g., 353 and 393 K, we have used[54] which is a classical molecular dynamic with a focus on material modelling. VMD (Visual Molecular Dynamics)[55] and OVITO[56] were used to visualize the MD trajectories of various structural configurations. The structural minimization was

performed using Polak-Ribiere version of the conjugate gradient (CG) algorithm coupled with NPT[57] (isothermal and isobaric) and NVT[58] (Langevin thermostat & production with Nose-Hoover) ensembles using Universal Force Field (UFF)[59] for all the structural configurations. The simulation was performed for 200 ps with a timestep of 1 fs. (Supplementary Video S1). Moreover, we have also analysed pair correlation function *g(r)* that accounts for the number of neighbors for each particle that are within a given cut-off range (in our case at r = 3.2) around its position by analyzing the structural stability at different temperatures.

The electronic properties of materials with different configurations were calculated by employing the GGA functional. The highest occupied molecular orbital (HOMO), lowest unoccupied molecular orbital (LUMO) energies of all compounds are presented in Table 1. The electronic absorption relates to the transition from the ground state to the first excited state and mainly described by one electron excitation from HOMO to LUMO.[60] The optical absorption coefficient have been extracted from the imaginary part of the complex dielectric function, $\varepsilon(\omega) = \varepsilon_r(\omega) + \varepsilon_i(\omega)$, where $\varepsilon_r(\omega)$ is the real part and $\varepsilon_i(\omega)$ is the imaginary part of the complex dielectric function.[61] The optical absorption coefficient is given as,

$$\alpha = \sqrt{2}\omega\sqrt{|\varepsilon(\omega)| - \varepsilon_r(\omega)}, \qquad (1)$$

Where, $|\varepsilon(\omega)| = \sqrt{\varepsilon_r^2(\omega) + \varepsilon_i^2(\omega)}$, is the relative dielectric constant.

ACKNOWLEDGMENT

S. G. thanks the French ministry of higher education for her PhD grant (doctoral school of chemistry, Lyon). Authors also thank L. Burel (TEM), Y. Aizac (PXRD), N. Bonnet (ICP elemental analysis) and Dr. L. Cardenas (XPS) of IRCELYON. D. S., P. K. D. and R. A. thank Olle Engkvists stiftelse, Carl Tryggers Stiftelse for Vetenskaplig Forskning (CTS) and the Swedish Research Council (VR) for financial support.

REFERENCES

(1) a) Chen, X.; Yang, J.; Wu, T.; Li, L.; Luo, W.; Jiang, W.; Wang, L. Nanostructured binary copper chalcogenides: synthesis strategies and common applications. *Nanoscale* **2018**, *10*, 15130–15163; b) Coughlan, C.; Ibáñez, M.; Dobrozhan, O.; Singh, A.; Cabot, A.; Ryan, K. M. Compound Copper Chalcogenide Nanocrystals. *Chem. Rev.* **2017**, *117*, 5865-6109.

(2) a) Xue, J.; Liu, J.; Liu, Y.; Li, H.; Wang, Y.; Sun, D.; Wang, W.; Huang, L.; Tang. J. Recent advances in synthetic methods and applications of $Ag_2S$-based heterostructure photocatalysts. *J. Mater. Chem. C* **2019**, *7*, 3988--4003; b) Gui, R.; Jin, H.; Wang, Z.; Tan, L. Recent advances in synthetic methods and applications of colloidal silver chalcogenide quantum dots. *Coord. Chem. Rev.* **2015**, *296*, 91-124.

(3) a) Wang, X.; Qiu, P.; Zhang, T.; Ren, D.; Wu, L.; Shi, X.; Yang, J.; Chen. L. Compound defects and thermoelectric properties in ternary CuAgSe-based materials. *J. Mater. Chem. A* **2015**, *3*, 13662-13670; b) Qiu, P. F.; Wang, X. B.; Zhang, T. S.; Shi, X.; Chen, L. D. Thermoelectric properties of Te-doped ternary CuAgSe compounds. *J. Mater. Chem. A* **2015**, *3*, 22454–22461.

(4) Han, C.; Sun, Q.; Cheng, Z. X.; Wang, J. L.; Li, Z.; Lu, G. Q.; Dou, S. X. Ambient Scalable Synthesis of Surfactant-Free Thermoelectric CuAgSe Nanoparticles with Reversible Metallic-*n*-*p* Conductivity Transition. *J. Am. Chem. Soc.* **2014**, *136*, 17626-17633.

(5) Gahlot, S.; Dappozze, F.; Singh, D.; Ahuja, R.; Cardenas, L.; Burel, L.; Amans, D.; Guillard, C.; Mishra, S. Room-temperature conversion of $Cu_{2-x}Se$ to CuAgSe nanoparticles to enhance photocatalytic performance of their composites with $TiO_2$, *Dalton Trans.* **2020**, *49*, 3580–3591.

(6) a) Savory, C. N.; Ganose, A. M.; Travis, W.; Atri, R. S.; Palgravec, R. G.; Scanlon, D. O. An assessment of silver copper sulfides for photovoltaic applications: theoretical and experimental insights, *J. Mater. Chem. A* **2016**, *4*, 12648–12657; b) Liu, Z.; Han, J.; Guo, K.; Zhang, X.; Hong, T. Jalpaite $Ag_3CuS_2$: A novel promising ternary sulfide absorber material for solar cells, *Chem. Commun.* **2015**, *51*, 2597—2600.

(7) Baker, C. L.; Lincoln, F. J.; Johnson, A. W. S. Crystal Structure Determination of $Ag_3CuS_2$ from Powder X-Ray Diffraction Data, *Aust. J. Chem.* **1992**, *45*, 1441-1449.

(8) Mi, L.; Wei, W.; Zheng, Z.; Zhu, G.; Hou, H.; Chen, W.; Guan, X. $Ag^+$ insertion into 3D hierarchical rose-like $Cu_{1.8}Se$ nanocrystals with tunable band gap and morphology genetic. *Nanoscale* **2014**, *6*, 1124-1133.

(9) Bryks, W.; Smith, S. C.; Tao, A. R. Metallomesogen Templates for Shape Control of Metal Selenide Nanocrystals. *Chem. Mater.* **2017**, *29*, 3653-3662.

(10) Wang, Y.; Li, X.; Xu, M.; Wang, K.; Zhu, H.; Zhao, W.; Yan, J.; Zhang, Z. Pressure induced photoluminescence modulation in a wide range and synthesis of monodispersed ternary AgCuS nanocrystal based on $Ag_2S$ nanocrystals, *Nanoscale* **2018**, *10*, 2577-2587.

(11) Brutchey, R. L. Diorganyl Dichalcogenides as Useful Synthons for Colloidal Semiconductor Nanocrystals. *Acc. Chem. Res.* **2015**, *48*, 2918-2926.

(12) Guo, Y.; Alvarado, S. R.; Barclay, J. D.; Vela, J. Shape-Programmed Nanofabrication: Understanding the Reactivity of Dichalcogenide Precursors. *ACS Nano* **2013**, *7*, 3616-3626.

(13) Kisker, D. W.; Steigerwald, M. L.; Kometani, T. Y.; Jeffers, K. S. Low-temperature organometallic vapor phase epitaxial growth of CdTe using a new organotellurium source. *Appl. Phys. Lett.* **1987**, *50*, 1681-1683.

(14) Chu, J. Y. C.; Lewicki, J. W. Thermal decomposition of bis(diphenylmethyl) diselenide. *J. Org. Chem*. 1977, *42*, 2491-2493.

(15) Chu, J. Y. C.; Marsh, D. G.; Günther, W. H. H. Photochemistry of organochalcogen compounds. I. Photolysis of benzyl diselenide. *J. Am. Chem. Soc.* **1975**, *97*, 4905-4908.

(16) a) Shen, G.; Chen, M.; Guyot-Sionnest, P.; Synthesis of Nonaggregating HgTe Colloidal Quantum Dots and the Emergence of Air-Stable n-Doping, *J. Phys. Chem. Lett.* **2017**, *8*, 2224−2228; b) Zhou, B.; Li, M.; Wu, Y.; Yang, C.; Zhang, W.-H.; Li, C. Monodisperse $AgSbS_2$ Nanocrystals: Size-Control Strategy, Large-Scale Synthesis, and Photoelectrochemistry, *Chem. Eur. J.* **2015**, *21*, 11143–11151; c) Zhang, J.; Gao, J.; Miller, E. M.; Luther, J. M.; Beard, M. C. Diffusion-Controlled Synthesis of PbS and PbSe Quantum Dots with in Situ Halide Passivation for Quantum Dot Solar Cells, *ACS Nano* **2014**, *8*, 614–622.

(17) Chang, Y.-P.; Hector, A. L.; Levason, W.; Reid, G.; Whittam, J. Synthesis and properties of $MoCl_4$ complexes with thio- and seleno-ethers and their use for chemical vapour deposition of $MoSe_2$ and $MoS_2$ films. *Dalton Trans*. **2018**, *47*, 2406-2414.

(18) Gurnani, C.; Hawken, S. L. Hector, A. L.; Huang, R.; Jura, M.; Levason, W.; Perkins, J.; Reid, G.; Stenning, G. B. G. Tin(IV) chalcogenoether complexes as single source precursors for the chemical vapour deposition of $SnE_2$ and SnE (E = S, Se) thin films. *Dalton Trans.* **2018**, *47*, 2628-2637.

(19) Chang, Y.-P.; Hector, A. L.; Levason, W.; Reid, G. Chalcogenoether complexes of Nb(V) thio- and seleno-halides as single source precursors for low pressure chemical vapour deposition of $NbS_2$ and $NbSe_2$ thin films. *Dalton Trans.* **2017**, *46*, 9824-9832.

(20) George, K. de Groot, C. H.; Gurnani, C.; Hector, A. L.; Huang, R.; Jura, M.; Levason, W.; Reid, G.; Telluroether and Selenoether Complexes as Single Source Reagents for Low Pressure Chemical Vapor Deposition of Crystalline $Ga_2Te_3$ and $Ga_2Se_3$ Thin Films. *Chem. Mater.* **2013**, *25*, 1829-1836.

(21) Sparks, J. R.; He, R; Healy, N.; Krishnamurthi, M.; Peacock, A. C.; Sazio, P. J. A.; Gopalan, V.; Badding, J. V. Zinc Selenide Optical Fibers. *Adv. Mater.* **2011**, *23*, 1647-1651.

(22) Boscher, N. D.; Carmalt, C. J.; Hyett, G.; Prieto, A. G.; Pankhurst, Q. A.; Parkin, I. P. Chromium oxyselenide solid solutions from the atmospheric pressure chemical vapour deposition of chromyl chloride and diethylselenide. *J. Mater. Chem.* **2008**, *18*, 1667-1673.

(23) Chang, Y.-P.; Levason, W.; Reid, G. Developments in the chemistry of the hard early metals (Groups 1–6) with thioether, selenoether and telluroether ligands. *Dalton Trans.* **2016**, *45*, 18393-18416.

(24) Kohyama, Y.; Murase, T.; Fujita, M. Control of silver(I)-dialkyl chalcogenide coordination by a synthetic cavity. *Angew. Chem. Int. Ed.* **2014**, *53*, 11510-11513.

(25) Levason, W.; Reid, G.; Zhang, W. The chemistry of the p-block elements with thioether, selenoether and telluroether ligands. *Dalton Trans.* **2011**, *40*, 8491-8506.

(26) Levason, W.; Orchard, S. D.; Reid, G. Recent developments in the chemistry of selenoethers and telluroethers. *Coord. Chem. Rev.* **2002**, *225*, 159-199.

(27) Gahlot, S.; Jeanneau, E.; Dappozze, F.; Guillard, C.; Mishra, S. Precursor-mediated synthesis of $Cu_{2-x}Se$ nanoparticles and its composites with $TiO_2$ for improved photocatalysis. *Dalton Trans.* **2018**, *47*, 8897–8905.

(28) Mishra, S.; Du, D.; Jeanneau, E.; Dappozze, F.; Guillard, C.; Zhang, J.; Daniele, S. A facile molecular precursor-based synthesis of $Ag_2Se$ nanoparticles and its composites with $TiO_2$ for enhanced photocatalytic activity. *Chem. Asian J.* **2016**, *11*, 1658-1663.

(29) Fang, C.; Zhang, S.; Zuo, P.; Wei, W.; Jin, B.; Wu, J.; Tian, Y. Nanotube–nanotube transformation synthesis and electrochemistry of crystalline CuAgSe nanotubes. *J Cryst Growth* **2009**, *311*, 2345-2351.

(30) Biesinger, M. C. Advanced analysis of copper X-ray photoelectron spectra, *Surf. Interface Anal.* **2017**, *49*, 1325-1334.

(31) Mishra, S.; Daniele, S. Metal-organic derivatives with fluorinated ligands as precursors for inorganic nanomaterials. *Chem. Rev.* **2015**, *115*, 8379-8448.

(32) Mishra, S.; Zhang, J.; Hubert-Pfalzgraf, L. G.; Luneau, D.; Jeanneau, E. The Interplay between yttrium, barium or copper trifluoroacetates and *N*-methyldiethanolamine: Synthesis of a heterometallic $Y_3Cu$ trifluoroacetate complex and a homometallic Ba-TFA 1D polymer. *Eur. J. Inorg. Chem.* **2007**, 602-608.

(33) Ayadi, H.; Fang, W.; Mishra, S.; Jeanneau, E.; Ledoux, G.; Zhang, J.; Daniele, S.; Influence of $Na^+$ ion doping on the phase change and upconversion emissions of the $GdF_3$: $Yb^{3+}$, $Tm^{3+}$ nanocrystals obtained from the designed molecular precursors. *RSC Adv.* **2015**, *5*, 100535-100545.

(34) Mishra, S.; Jeanneau, E.; Bulin, A.-L.; Ledoux, G.; Jouguet, B.; Amans, D.; Belsky, A.; Daniele, S.; Dujardin, C.; A molecular precursor approach to monodisperse scintillating $CeF_3$ nanocrystals. *Dalton Trans.* **2013**, *42*, 12633-12643.

(35) Mishra, S.; Jeanneau, E.; Daniele, S. Dimethyl selenide complexes of copper, gallium and indium halides as potential precursors for selenium-containing chalcopyrite semiconducting materials. *Polyhedron* **2010**, *29*, 500-506.

(36) Jura, M.; Levason, W.; Ratnani, R.; Reid, G.; Webster, M. Six- and eight-coordinate thio- and seleno-ether complexes of $NbF_5$ and some comparisons with $NbCl_5$ and $NbBr_5$ adducts, *Dalton Trans.* **2010**, *39*, 883–891.

(37) Lu, H.; Brutchey, R. L. Tunable Room-Temperature Synthesis of Coinage Metal Chalcogenide Nanocrystals from N-Heterocyclic Carbene Synthons, *Chem. Mater.* **2017**, *29*, 1396−1403.

(38) Fard, M. A.; Weigend, F.; Corrigan, J. F. Simple but effective: thermally stable Cu–$ESiMe_3$ *via* NHC ligation, *Chem. Commun.* **2015**, *51*, 8361-8364.

(39) Jones, A. C.; Hitchman, M. L. Chemical Vapour Deposition: Precursors, Processes and Applications, Royal Society of Chemistry, 2009.

(40) Mehlana, G.; Bourne, S. A. Unravelling chromism in metal–organic frameworks. *CrystEngComm* **2017**, *19*, 4238-4259.

(41) Setifi, F.; Benmansour, S.; Marchivie, M.; Dupouy, G.; Triki, S.; Sala-Pala, J.; Salaün, J.-Y.; Gómez-García, C. J.; Pillet, S.; Lecomte, C.; Ruiz, E.; Bistability, M. Thermochromism in a Molecular $Cu^{II}$ Chain. *Inorg. Chem.* **2009**, *48*, 1269-1271.

(42) de Almeida, K. J.; Ramalho, T. C.; Rinkevicius, Z.; Vahtras, O.; Ågren, H.; Cesar, A. Theoretical Study of Specific Solvent Effects on the Optical and Magnetic Properties of Copper(II) Acetylacetonate. *J. Phys. Chem. A* **2011**, *115*, 1331-1339.

(43) CrysAlisPro Software System, Rigaku Oxford Diffraction, 2018.

(44) Clark, R. C.; Reid, J. S. The analytical calculation of absorption in multifaceted crystals. *Acta Crystallogr. Sect. A: Found. Crystallogr.* **1995**, *51*, 887–897.

(45) Sheldrick, G. M. ShelXT-Integrated space-group and crystal-structure determination, *Acta Cryst.* **2015**, *A71*, 3-8.

(46) Dolomanov, O. V.; Bourhis, L. J.; Gildea, R. J.; Howard, J. A. K.; Puschmann, H. Olex2: A complete structure solution, refinement and analysis program, *J. Appl. Cryst.* **2009**, *42*, 339-341.

(47) Sheldrick, G. M. Crystal structure refinement with ShelXL. *Acta Cryst.* **2015**, *C27*, 3-8.

(48) Kresse, G.; Furthmüller, J. Efficient Iterative Schemes for Ab Initio Total-Energy Calculations Using a Plane-Wave Basis Set. *Phys. Rev. B* **1996**, *54*, 11169–11186.

(49) Kohn, W. Density Functional and Density Matrix Method Scaling Linearly with the Number of Atoms. *Phys. Rev. Lett.* **1996**, *76*, 3168–3171.

(50) Kohn, W.; Sham, L. J. Self-Consistent Equations Including Exchange and Correlation Effects. *Phys. Rev.* **1965**, *140*, A1133–A1138.

(51) Kresse, G.; Joubert, D. From Ultrasoft Pseudopotentials to the Projector Augmented-Wave Method. *Phys. Rev. B* **1999**, *59*, 1758–1775.

(52) Perdew, J. P.; Burke, K.; Ernzerhof, M. Generalized Gradient Approximation Made Simple. *Phys. Rev. Lett.* **1996**, *77*, 3865–3868.

(53) Monkhorst, H. J.; Pack, J. D. Special Points for Brillouin-Zone Integrations. *Phys. Rev. B* **1976**, *13*, 5188–5192.

(54) Majure, D. L.; Haskins, R. W.; Lee, N. J.; Ebeling, R. M.; Maier, R. S.; Marsh, C. P.; Bednar, A. J.; Kirgan, R. A.; Welch, C. R.; Cornwell, C. F. Large-Scale Atomic/Molecular Massively Parallel Simulator (LAMMPS) Simulations of the Effects of Chirality and Diameter on the Pullout Force in a Carbon Nanotube Bundle. In *2008 DoD HPCMP Users Group Conference*; IEEE, 2008; pp 201–207.

(55) Humphrey, W.; Dalke, A.; Schulten, K. VMD: Visual Molecular Dynamics. *J. Mol. Graph.* **1996**, *14*, 33–38.

(56) Stukowski, A. Visualization and Analysis of Atomistic Simulation Data with OVITO–the Open Visualization Tool. *Model. Simul. Mater. Sci. Eng.* **2010**, *18*, 015012.

(57) Melchionna, S.; Ciccotti, G.; Lee Holian, B. Hoover NPT Dynamics for Systems Varying in Shape and Size. *Mol. Phys.* **1993**, *78*, 533–544.

(58) Tobias, D. J.; Martyna, G. J.; Klein, M. L. Molecular Dynamics Simulations of a Protein in the Canonical Ensemble. *J. Phys. Chem.* **1993**, *97*, 12959–12966.

(59) Rappe, A. K.; Casewit, C. J.; Colwell, K. S.; Goddard, W. A.; Skiff, W. M. UFF, a Full Periodic Table Force Field for Molecular Mechanics and Molecular Dynamics Simulations. *J. Am. Chem. Soc.* **1992**, *114*, 10024–10035.

(60) Saravanan, S.; Balachandran, V. Quantum Chemical Studies, Natural Bond Orbital Analysis and Thermodynamic Function of 2, 5-Dichlorophenylisocyanate. *Spectrochim. Acta Part A Mol. Biomol. Spectrosc.* **2014**, *120*, 351–364.

(61) Singh, D.; Gupta, S. K.; Sonvane, Y.; Lukačević, I. Antimonene: A Monolayer Material for Ultraviolet Optical Nanodevices. *J. Mater. Chem. C* **2016**, *4*, 6386–6390.

ASSOCIATED CONTENT

**Supporting Information**. FT-IR of **1**-**4**, X-ray structures of **2** and **3**, TG-DTG curves of **3** and **4**, additional XRD, SEM, TEM, HR-TEM, EDX and XPS analysis of AgCuSe and $Ag_3CuS_2$, additional simulated figures of **1**-**4**, videos of simulated structures of **1**-**4** and thermochromic behaviour of **1**. This material is available free of charge *via* the Internet at http://pubs.acs.org.

**Accession Codes**

CCDC1903337, 1903338, 1968807 and 1968808 contain the supplementary crystallographic data for this paper. These data can be obtained free of charge via www.ccdc.cam.ac.uk/data_request/cif, or by emailing data_request@ccdc.cam.ac.uk, or by contacting The Cambridge Crystallographic Data Centre, 12 Union Road, Cambridge CB2 1EZ, UK; fax: +44 1223 336033.

AUTHOR INFORMATION

**Corresponding Author**

* Shashank Mishra

e-mail: shashank.mishra@ircelyon.univ-lyon1.fr; Fax : (+33) 472445399.

**Author Contributions**

The manuscript was written through contributions of all authors. All authors have given approval to the final version of the manuscript.

**Notes**

The authors declare no competing financial interest.

**TOC graphic**

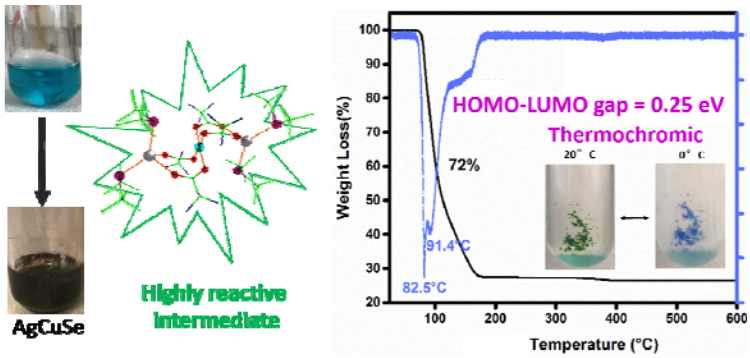


**TOC synopsis**

**Catch me if you can!** Successful isolation and characterization of a molecular intermediate species with extraordinary reactivity and interesting thermochromic properties establishes the route for the formation of AgCuSe nanoparticles at room temperature.